NANO LETTERS

pubs.acs.org/NanoLett Letter

Metasurface Enabled Photothermoelectric Photoresponse of Semimetal Cd_3As_2 for Broadband Photodetection

Zhaohang Xue,[#] Zipu Fan,[#] Xin Liao,[#] Yaolong Li, Yulu Qin, Guanyu Zhang, Xiaoming Song, Zhi-Min Liao,* Dong Sun,* Guowei Lu,* and Qihuang Gong

Cite This: *Nano Lett.* 2022, 22, 8728−8734 Read Online

ACCESS | Metrics & More | Article Recommendations | Supporting Information

ABSTRACT: The artificial engineering of photoresponse is crucial for optoelectronic applications, especially for photodetectors. Here, we designed and fabricated a metasurface on a semimetallic Cd_3As_2 nanoplate to improve its thermoelectric photoresponse. The metasurface can enhance light absorption, resulting in a temperature gradient. This temperature gradient can contribute to thermoelectric photoresponse through the photothermoelectric effect. Furthermore, power-dependent measurements showed a linearly dependent photoresponse of the Cd_3As_2 metasurface device, indicating a second-order photocurrent response. Wavelength-dependent measurements showed that the metasurface can efficiently separate photoexcited carriers in the broadband range of 488 nm to 4 μm. The photoresponse near the metasurface boundaries exhibits a responsivity of ∼1 mA/W, which is higher than that near the electrode junctions. Moreover, the designed metasurface device provided an anisotropic polarization-dependent photoresponse rather than the isotropic photoresponse of the original Cd_3As_2 device. This study demonstrates that metasurfaces have excellent potential for artificial controllable photothermoelectric photoresponse of various semimetallic materials.

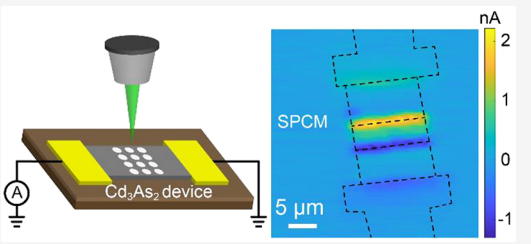

KEYWORDS: *Dirac semimetal, metasurface, photothermoelectric effect, photodetector*

The three-dimensional Dirac semimetal Cd_3As_2, a bulk analog of graphene, has attracted widespread attention because of its ultrahigh carrier mobility and gapless Dirac band structure.[1−3] Similar to graphene, Cd_3As_2 can be used in broadband photodetectors with a detection spectrum ranging from ultraviolet to long-wave infrared.[4,5] In contrast to monolayer graphene, which has an absorption coefficient of ∼2.3%,[6] the bulk characteristics of Cd_3As_2 endow it with a strong absorption capability and consequently better photoresponsivity. In addition, similar to graphene,[7,8] the Cd_3As_2 photodetector exhibits an ultrafast response up to the picosecond scale, as revealed by previous femtosecond pump−probe measurements.[9−11] Meanwhile, the oxidation layer on the surface of Cd_3As_2 provides good stability through isolation from the external environment.[12] Therefore, Cd_3As_2 is a promising material for high-performance photodetectors.

Owing to the metallic nature, external bias can lead to high dark currents in photodetectors based on semimetals.[13] Therefore, such photodetectors usually operate without external bias, which limits the charge separation of photoexcited carriers and subsequent photoresponsivity. In an unbiased photodetector, the nonzero photoresponse depends on the generation and subsequent separation of electron−hole (e−h) pairs.[14−16] The charge separation mechanism of the Cd_3As_2 photodetector primarily includes the photovoltaic (PV), photo-Dember (PD), and photothermoelectric (PTE) effects. Among these, the PV effect uses the built-in electric field induced by the work function difference between Cd_3As_2 and metal electrodes to separate the photoexcited e−h pairs, resulting in photovoltage.[17] The PD effect arises from the asymmetric diffusivity of photoexcited electrons and holes, which creates a transient spatial charge distribution and hence a voltage buildup.[18] However, the photoresponses of Cd_3As_2 photodetectors based on the PV or PD effect are adjacent to the metal electrode, which restricts the response area and potential applications of the photodetector. The PTE effect generated by the temperature gradient-induced electron diffusion rate difference also plays a critical role in the generation of the photoresponse of the Cd_3As_2 photodetector, as revealed by terahertz emission investigations.[19] The PTE effect enables the efficient harvesting of energy, high-efficiency photoelectric energy conversion, and photodetection.[20,21] Recent progress in the discovery of the topologically enhanced shift current response as an efficient charge separation mechanism has significantly boosted the development of photodetectors based on semimetallic materials, particularly in the mid-infrared range.[13,22] But such a charge separation

Received: September 10, 2022
Revised: October 24, 2022
Published: October 31, 2022

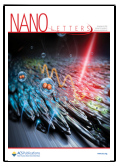

https://doi.org/10.1021/acs.nanolett.2c03574
Nano Lett. 2022, 22, 8728−8734

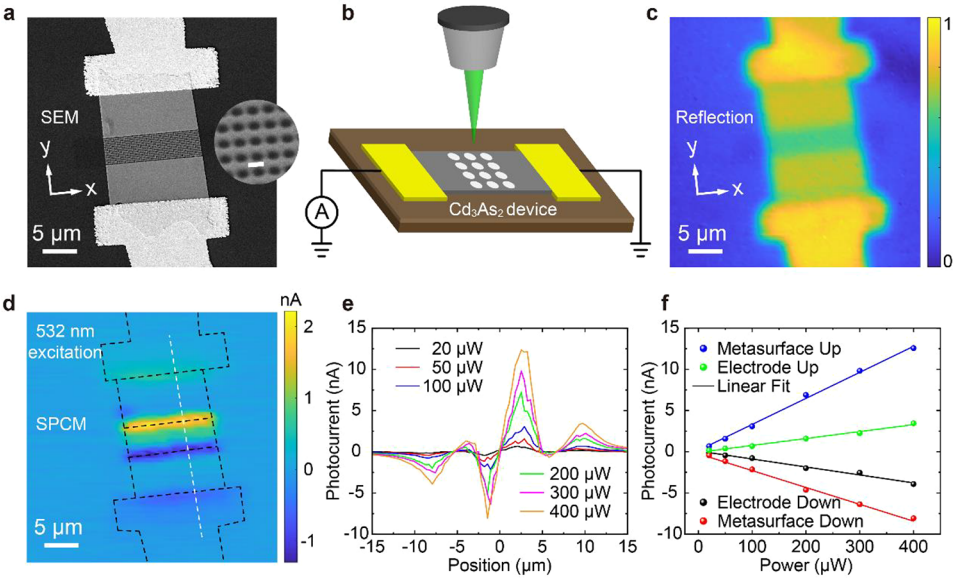

Figure 1. Photoresponse of the Cd_3As_2 metasurface device. (a) Scanning electron microscopy (SEM) image of the Cd_3As_2 metasurface device. The inset is an enlarged SEM image of the Cd_3As_2 metasurface, and the 250 nm scale bar manifests the metasurface period. (b) Schematic of scanning photocurrent measurement (SPCM). (c) Scanning optical reflection image of the device. (d) SPCM image of the device with an excitation power of 50 μW at 532 nm. The black dashed lines indicate the edges of electrodes, the Cd_3As_2 nanoplate, and Cd_3As_2 metasurface. Photoresponses occur in both metasurface boundaries and Cd_3As_2−electrode junctions. (e) Line-cut of the photoresponse along the white dashed line in part d under different excitation powers. (f) Power-dependent photoresponses of the four distinct response regions with linear fits.

mechanism is limited to inversion symmetry broken Weyl semimetals and does not apply to Dirac semimetals with inversion symmetry. Alternatively, the excellent thermoelectric properties of Dirac semimetal Cd_3As_2 and the flexible engineering of metasurfaces can induce efficient charge separation through the PTE effect, which can serve as an efficient charge separation mechanism for semimetal-based photodetectors.

In this study, we designed and fabricated a metasurface onto a Cd_3As_2 photodetector to artificially engineer its photoresponse. The absorption enhancement of the Cd_3As_2 metasurface results in temperature gradient distributions near the metasurface boundaries and generates thermoelectric photoresponses through the PTE effect. Power-dependent photocurrent measurements show that the Cd_3As_2 metasurface device has a linearly dependent photoresponse as a second-order effect. Moreover, wavelength-dependent photocurrent measurements illustrate that the metasurface can enhance the photoresponses over a broadband range from 488 nm to 4 μm. Particularly for 650 nm (1.91 eV) and 720 nm (1.72 eV) excitation, the photocurrent responsivities near the metasurface boundaries increased by 1 order of magnitude compared with those near the electrode junctions. The Cd_3As_2 metasurface device exhibited a responsivity of approximately 1 mA/W. Although Cd_3As_2 has a nearly isotropic photoresponse because of its centrosymmetric lattice,[23] the metasurface provides a linear polarization-dependent photoresponse with a ratio of anisotropy of ∼2.1. The metasurface makes it possible to develop polarization-sensitive photodetection for other noncentrosymmetric topological semimetals.[24−26] The measurements of photoemission electron microscopy (PEEM) showed higher photoemission on the Cd_3As_2 metasurface due to the higher electric field resulting from the interference of incident light and quasi-cylindrical waves (QCW).[27] Finite-difference time-domain (FDTD) simulations also show the absorption enhancement diagram of the Cd_3As_2 metasurface. These findings demonstrate the considerable potential of designing metasurfaces for an artificially controllable PTE photoresponse of photodetectors.

The Cd_3As_2 nanoplates were synthesized via the chemical vapor deposition (CVD) method.[12,28] The Au−Cd_3As_2−Au photodetectors were fabricated via electron-beam lithography (details in Figure S1). Subsequently, elaborately designed metasurface nanostructures were fabricated onto the middle of the Cd_3As_2 photodetector using the focused ion beam (FIB) milling system. Figure 1a shows a scanning electron microscopy (SEM) image of the Cd_3As_2 device with a metasurface, and the inset shows an enlarged SEM image of the metasurface structures. The metasurface had a period of 250 nm, and the size of the elliptical nanostructure was 180 nm × 120 nm. Raman spectra of the Cd_3As_2 nanoplates and metasurface confirm the high quality of the (112) surface plane of the Cd_3As_2 nanoplates (Figure S2). Figure 1b shows a schematic of the scanning photocurrent measurement (SPCM) of the Cd_3As_2 metasurface device operating at zero bias. A continuous wave (CW) 532 nm laser was focused on the Cd_3As_2 device, and photocurrent signals were recorded at each position on the sample. The resistance of the Cd_3As_2 metasurface device is ∼1124 Ω (Figure S2). Figure 1c shows the device's typical scanning reflection image at an excitation power of 50 μW at 532 nm. In the following photocurrent measurements, the polarization of the excitation laser was along the y direction unless otherwise stated. The significant decrease in the optical reflection intensity in the metasurface area was due to the enhanced absorption of the Cd_3As_2 metasurface.

Figure 1d shows the corresponding room-temperature SPCM image of the Cd_3As_2 metasurface device. The device's photoresponses occur primarily in the Cd_3As_2−electrode junctions and the metasurface boundaries. These photoresponses can be explained by the PV and PTE effects, respectively. Owing to the PV effect, a built-in electric field

https://doi.org/10.1021/acs.nanolett.2c03574
Nano Lett. 2022, 22, 8728−8734

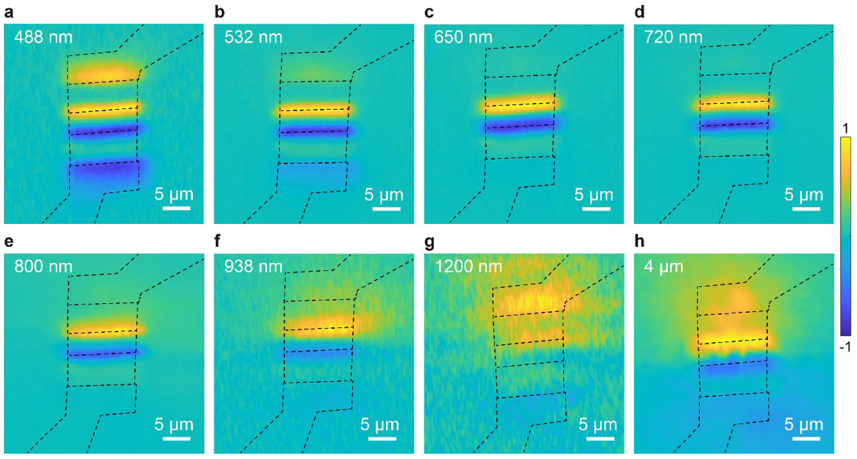

Figure 2. Broadband photoresponse enhancement on the Cd_3As_2 metasurface device. (a–h) Normalized SPCM images of the Cd_3As_2 metasurface device with excitations at 488 nm, 532 nm, 650 nm, 720 nm, 800 nm, 938 nm, 1200 nm, and 4 μm, respectively.

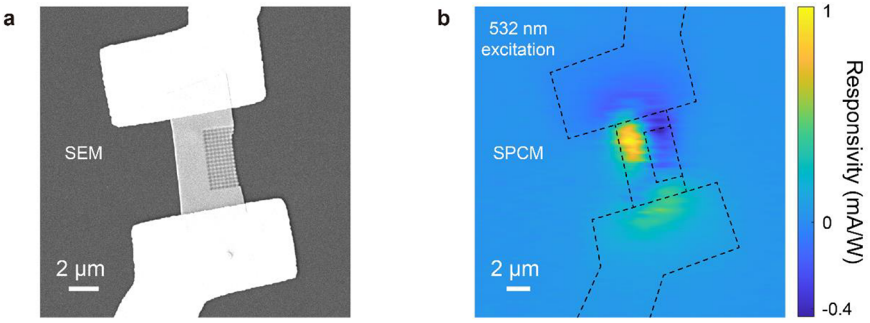

Figure 3. Photocurrent responsivity of the Cd_3As_2 half-etched metasurface device. SEM image (a) and responsivity (b) of the Cd_3As_2 half-etched metasurface device.

forms near the Cd_3As_2–electrode junctions because of the work function difference between Cd_3As_2 and Au electrodes. In addition, the PV effect separates the photogenerated e–h pairs forming photocurrents on the Cd_3As_2–electrode junctions.[17] For the PTE effect on the two metasurface boundaries, V_{PTE} is calculated by integrating the Seebeck coefficient with the temperature gradient: $V_{PTE} = \int S \cdot \nabla T \, dx$, where S represents the Seebeck coefficient and ∇T represents the temperature gradient between the regions with and without a metasurface. The optical absorption in the metasurface area increases, resulting in a higher temperature in the metasurface region than in the flat region. Moreover, the thermal conductivity at the etching Cd_3As_2 metasurface is lower, which depresses the heat conduction.[29,30] These factors result in distinct temperature gradients and PTE photoresponses at the metasurface boundaries. Furthermore, the inverse directions of the temperature gradients cause the inversion of photocurrents at the metasurface boundaries.

To quantify the photoresponses, Figure 1e plots them along the white dashed line in Figure 1d. The photoresponses present four distinct response regions: the electrode bottom, electrode top, metasurface boundary bottom, and metasurface boundary top. The photoresponses increased linearly when the laser power increased from 20 to 400 μW (Figure 1f), indicating that the PV and PTE effects have a constant conversion efficiency as a second-order effect.[31] The photoresponses caused by the PTE effect are nearly 4 times those caused by the PV effect under 532 nm excitation with different incident powers.

Moreover, we measured the wavelength-dependent photoresponse of the Cd_3As_2 metasurface device and verified that the charge separation is efficient regardless of the excitation wavelength. As demonstrated in our previous work,[27] the density of free carriers in the Cd_3As_2 is too low to support plasmonic resonance in the visible or ultraviolet range. The semimetal Cd_3As_2 does not support plasmonic resonance as metal materials. The Cd_3As_2 photodetector exhibits a broadband photoresponse, which benefits from the gapless linear dispersion band structure with ultrahigh mobility.[2,3,32] The broadband Cd_3As_2 photodetector working in visible and infrared ranges has great potential in many applications.[33]

The wavelength-dependent SPCM results, shown in Figure 2a–h, indicate that the Cd_3As_2 metasurface device exhibits broadband photoresponses from 488 nm to 4 μm. The SEM image, scanning reflection image, and I–V curve of this device are shown in Figure S2. The Cd_3As_2 exhibits stronger light absorption in the ultraviolet band.[34] The device exhibits stronger PV photoresponses at shorter wavelengths (maximum responsivity occurs under 488 nm excitation, Figure S3). In addition, the metasurface boundaries exhibit improved photoresponses compared with the electrode junctions in broadband. Particularly for 650 nm (1.91 eV) and 720 nm (1.72 eV) excitation, the responsivities increased by 1 order of magnitude (Figure S3).

The responsivity of the device (Figure S3) is ~40 μA/W, which is lower than that (5.9 mA/W) reported in our previous study.[17] As mentioned above, the increased resistance of the metasurface device can partially explain the lower responsivity.

https://doi.org/10.1021/acs.nanolett.2c03574
Nano Lett. 2022, 22, 8728–8734

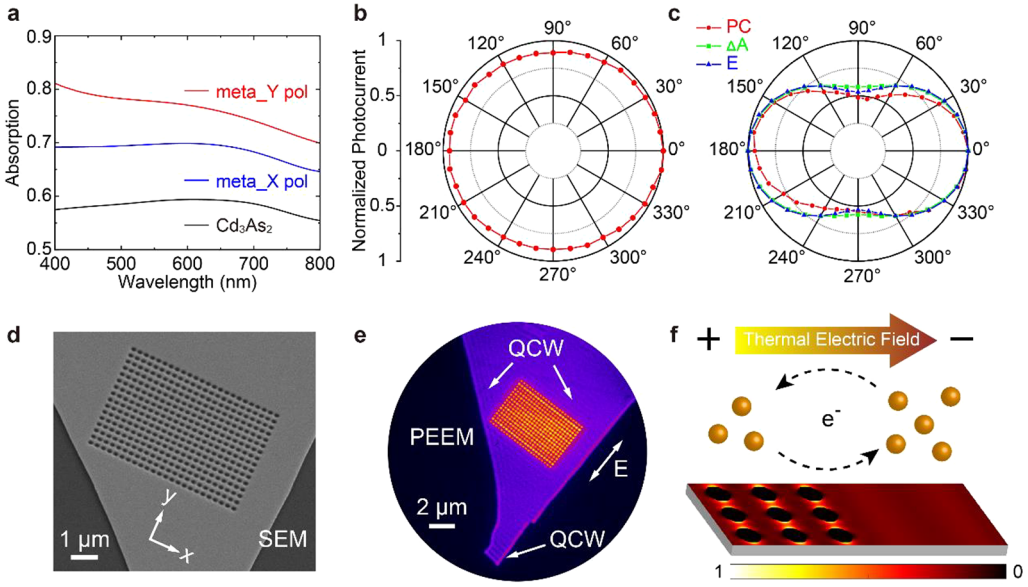

Figure 4. (a) Absorption enhancement of the Cd_3As_2 metasurface under x and y polarization compared with the original Cd_3As_2 nanoplate. (b) Normalized isotropic photoresponse for the Cd_3As_2−electrode junction. (c) Normalized anisotropic photoresponse, absorption difference, and electric field for the Cd_3As_2 metasurface. (d) SEM image of the Cd_3As_2 metasurface. (e) PEEM image of the Cd_3As_2 metasurface and optical QCW. (f) Normalized FDTD simulated absorption diagram of the Cd_3As_2 metasurface and nanoplate, with the schematic of the PTE effect.

We speculate that the increase in device resistance is caused by the FIB milling holes and edge roughness of the Cd_3As_2 metasurface device. Thus, the increase in resistance restricts the responsivity of the photodetector. We designed and fabricated a half-etched metasurface device to verify the influence of milling holes on photoresponsivity (Figure 3a). Half of the device was etched into the metasurface while retaining half of the original nanoplate. Interestingly, the responsivity of the half-etched device could reach ∼1 mA/W (Figure 3b), which is of the same magnitude as that of the previous device. Notably, the responsivity near the metasurface boundaries was higher than that near the electrode junctions in the same device. That indicates that the metasurface structure can still provide an efficient charge separation mechanism through the thermoelectric photoresponse. However, more efforts are required to understand the lower responsivity of the present metasurface device thoroughly to the previous pure nanoplate device.

Next, we performed numerical calculations using the FDTD method to understand how the metasurface affected the photothermal response of the devices. As shown in Figure 4a, the absorption of the Cd_3As_2 metasurface can reach 80% (under y polarization) and 70% (under x polarization). That is higher than the original Cd_3As_2 nanoplate (∼60%). The Cd_3As_2 metasurface also exhibits broadband absorption similar to the original Cd_3As_2 nanoplate because of the gapless Dirac band structure.[2,3,32] Owing to the centrosymmetric lattice of Cd_3As_2,[23] the photoresponse at the Cd_3As_2−electrode junction is nearly isotropic (Figure 4b). Interestingly, the photoresponse at the metasurface boundary was anisotropic by tuning the linear polarization of the 532 nm excitation laser (Figure 4c). The ratio of anisotropy (maximum/minimum) was approximately 2.1. In the FDTD simulation, absorption differences ($\Delta A = A_{metasurface} - A_{nanoplate}$) and electric field on the metasurface show anisotropic features owed to the asymmetry of metasurface nanostructures. The Cd_3As_2 metasurface exhibited a higher electric field under y polarization (0°), corresponding to stronger light absorption, a higher temperature gradient, and a larger PTE photoresponse. Thus, the periodic elliptical metasurface introduces asymmetry to the centrosymmetric Cd_3As_2, resulting in polarization-sensitive photodetection based on isotropic materials.

Furthermore, we investigated the local electric-field distribution on the Cd_3As_2 metasurface using PEEM. The PEEM is a nonscanning high-spatial-resolution instrument that collects photoelectrons to image.[35,36] The PEEM is a powerful tool for investigating photonic modes, including surface plasmon polaritons,[37,38] dielectric waveguides,[39,40] and QCW modes.[27] In our previous work,[9] we demonstrated that the photoemission intensity of Cd_3As_2 is proportional to the electric field intensity. The increased electric field contributes to optical absorption. Therefore, the local electric-field distribution indirectly reflects the light absorption enhancement, then the local temperature distribution of the Cd_3As_2 metasurface. Figure 4d shows an SEM image of the Cd_3As_2 metasurface, and its FIB etching parameters are consistent with those in Figure 1a. Figure 4e shows a static PEEM image of the Cd_3As_2 metasurface under 410 nm laser excitation with y polarization. The TM-mode (p-polarization) optical QCW was excited from the edges of the nanoplate and metasurface. As a result, the photoemission intensity of the Cd_3As_2 metasurface was more substantial than that of the original Cd_3As_2 nanoplate. Figure S4 shows the corresponding FDTD simulated near-field electric field distribution on the Cd_3As_2 metasurface, which agrees with the PEEM image. The photoemission intensity of the Cd_3As_2 metasurface under a 410 nm laser with x polarization is approximately half that with y polarization. The anisotropic photoemission intensity follows the anisotropic absorption and electric field distribution shown in Figure 4c. These results confirm that the metasurface can optimize the local field and improve photodetector performance.

An enhanced near field can result in higher optical absorption. Then, the different absorption leads to a

https://doi.org/10.1021/acs.nanolett.2c03574
Nano Lett. 2022, 22, 8728−8734

temperature gradient distribution between the Cd_3As_2 metasurface and the original Cd_3As_2 nanoplate. Metasurface-enhanced light absorption has also been reported in the previous literature.[41,42] Figure 4f shows a normalized FDTD simulated absorption diagram of the Cd_3As_2 nanoplate with and without a metasurface, presenting a temperature gradient distribution around the boundary. In the n-doped Dirac semimetal, the majority of carriers (electrons) diffuse from the hot-side metasurface to the cold-side original nanoplate. The thermal electric field is established from the unbalanced carrier gradient, which is the mechanism of the PTE effect modified by the metasurface in the present device.

The metasurface region contains fewer materials in volume but possesses a higher optical absorption, which is counter-intuitive. We explain it as follows: the light absorption of the device is proportional to $\alpha \cdot E^2 \cdot V_{eff}$, where α represents the intrinsic light absorption rate of Cd_3As_2, E represents the electric field, and V_{eff} represents the effective light absorption volume. From the FDTD simulated electric field distribution and absorption diagram (Figure S5), the light absorption is restricted within a depth of ∼20 nm for the original Cd_3As_2 nanoplate. As the thickness of the Cd_3As_2 nanoplate was ∼100 nm, the original nanoplate was not fully involved in the optical absorption. For the Cd_3As_2 metasurface, the simulated electric field penetrated the nanoplate, and the deep part of Cd_3As_2 was involved in light absorption (Figure S5). Although the etched metasurface only accounts for ∼73% of the volume of the original nanoplate, the metasurface nanostructures increase V_{eff} by ∼40%, which can enhance the light-confinement capability.[43] Moreover, the electric field E on the metasurface is enhanced because of the interference of incident light and QCW, as demonstrated by the PEEM measurements in Figure 4e. Synthetically considering V_{eff} and E, the absorption of the Cd_3As_2 metasurface was enhanced compared with that of the original nanoplate. The metasurface absorption enhancement also agrees with the decrease in the reflection intensity, as shown in Figure 1c. Furthermore, the etched Cd_3As_2 metasurface has a lower thermal conductivity than the original Cd_3As_2 nanoplate.[29,30] All of these factors can result in a distinct temperature gradient at the metasurface boundary. Therefore, the thermoelectric photoresponse was established efficiently from the temperature gradient through the PTE effect.

The parameters of the metasurface were carefully optimized after extensive computational simulation. We investigated the effects of the shape and period on the absorption of the Cd_3As_2 metasurface (Figure S6). We chose the elliptical shape for the metasurface after comparing rectangular, elliptical, square, and circular shapes (Figure S6a). The metasurface-enhanced absorption was optimized by comparing various periods (Figure S6b). We chose 250 nm as the period of the metasurface because it results in a more significant absorption enhancement.[44]

In conclusion, we designed and fabricated a metasurface on a Cd_3As_2 photodetector device. The metasurface can artificially engineer the photoresponse with an efficient charge separation mechanism through the photothermoelectric effect. The metasurface provides a way to design active optical sensitive areas and exhibits broadband-enhanced photoresponses from 488 nm to 4 μm. The power-dependent photocurrent measurements showed the linearly dependent photoresponses of the Cd_3As_2 metasurface device, with a maximum responsivity of approximately 1 mA/W. The metasurface provided a linear polarization-dependent photoresponse with a ratio of anisotropy of ∼2.1 to the centrosymmetric lattice Cd_3As_2. The numerical and experimental results confirmed that the metasurface could enhance optical absorption, which results in a large temperature gradient distribution. Thus, the PTE effect generates the thermal electric field on the device. These findings enabled us to engineer the PTE photoresponse of photodetectors by artificial metasurfaces.

METHODS

Sample Characterization and Device Fabrication. In our previous study,[9,27] the synthesis process, energy-dispersive X-ray spectroscopy (EDS), Raman spectroscopy, atomic force microscopy (AFM), and spectroscopic ellipsometry characterizations of the Cd_3As_2 nanoplates were discussed in detail. The synthesized Cd_3As_2 nanoplates were transferred to a Si substrate with a 285-nm-thick SiO_2 layer using an XYZ micromanipulator. The Au−Cd_3As_2−Au device was fabricated using e-beam lithography and evaporation (Figure S1 in the detailed process). Then, elaborately designed metasurface nanostructures were etched using an SEM/FIB milling system (Zeiss Crossbeam 540). The etching parameters were 30 kV and 20 pA with a dose factor of 10. SEM images were acquired after FIB etching.

PEEM Measurement. PEEM measurements were performed using a high-resolution PEEM system (SPELEEM, Elmitec GmbH) equipped with an aberration corrector. The etched Cd_3As_2 nanoplates were transferred to the PEEM preparation chamber and annealed under an ultrahigh vacuum (below 5×10^{-9} Torr) at 180 °C for 1 h to remove any H_2O or impurities absorbed on the sample surface. Then, 410- and 532-nm femtosecond laser pulses were focused on the sample at normal incidence. The excited photoelectrons were collected by a 20 kV static electric field between the sample and the main objective lens of the PEEM. Photoelectrons were emitted onto the fluorescent screen to generate PEEM images with a maximum spatial resolution of ∼10 nm.

Scanning Photocurrent Measurements. In our previous study,[17,24,25] the setup of SPCMs was described in detail. In this study, standard SPCMs were performed using a 532 nm CW laser with a spatial resolution of ∼1 μm. The laser beam was focused using a 50× transmissive objective lens, and a scanning mirror was used to scan the light beam on the sample. The laser beam was modulated using a mechanical chopper (379 Hz), and the short-circuit photocurrent signal was detected using a lock-in amplifier. The reflection signal and photocurrent responses were recorded simultaneously to obtain reflection and photocurrent mapping.

For wavelength-dependent measurements, several bandpass filters were used to select the desired wavelength from the white-light supercontinuum output of Fianium: WhiteLase-Micro (20 MHz, 6 ps, 450−2200 nm). A CW quantum cascade laser source emitting at 4 μm was used for mid-infrared measurements. The mid-infrared beam was focused using a 40× reflection objective lens with a spot diameter of approximately 8 μm.

A motorized rotation stage was used to rotate a half-waveplate for linear polarization-dependent measurements.

All SPCMs were performed in an unbiased self-powered mode at room temperature.

https://doi.org/10.1021/acs.nanolett.2c03574
Nano Lett. 2022, 22, 8728−8734

■ ASSOCIATED CONTENT

Supporting Information

The Supporting Information is available free of charge at https://pubs.acs.org/doi/10.1021/acs.nanolett.2c03574.

Fabrication of Cd_3As_2 device, Cd_3As_2 metasurface device characterizations, photocurrent responsivity, PEEM image of Cd_3As_2 metasurface and optical QCW, simulated electric field distribution and absorption diagram, absorption of Cd_3As_2 metasurface with different shapes and periods (PDF)

■ AUTHOR INFORMATION

Corresponding Authors

Zhi-Min Liao − *State Key Laboratory for Mesoscopic Physics, Collaborative Innovation Center of Quantum Matter, Frontiers Science Center for Nano-Optoelectronics, School of Physics, Peking University, Beijing 100871, China;* orcid.org/0000-0001-6361-9626; Email: liaozm@pku.edu.cn

Dong Sun − *International Center for Quantum Materials, School of Physics, Peking University, Beijing 100871, China;* orcid.org/0000-0002-0898-4548; Email: sundong@pku.edu.cn

Guowei Lu − *State Key Laboratory for Mesoscopic Physics, Collaborative Innovation Center of Quantum Matter, Frontiers Science Center for Nano-Optoelectronics, School of Physics, Peking University, Beijing 100871, China; Collaborative Innovation Center of Extreme Optics, Shanxi University, Taiyuan, Shanxi 030006, China; Peking University Yangtze Delta Institute of Optoelectronics, Nantong, Jiangsu 226010, China;* orcid.org/0000-0003-0646-6971; Email: guowei.lu@pku.edu.cn

Authors

Zhaohang Xue − *State Key Laboratory for Mesoscopic Physics, Collaborative Innovation Center of Quantum Matter, Frontiers Science Center for Nano-Optoelectronics, School of Physics, Peking University, Beijing 100871, China*

Zipu Fan − *International Center for Quantum Materials, School of Physics, Peking University, Beijing 100871, China*

Xin Liao − *State Key Laboratory for Mesoscopic Physics, Collaborative Innovation Center of Quantum Matter, Frontiers Science Center for Nano-Optoelectronics, School of Physics, Peking University, Beijing 100871, China;* orcid.org/0000-0001-8045-3795

Yaolong Li − *State Key Laboratory for Mesoscopic Physics, Collaborative Innovation Center of Quantum Matter, Frontiers Science Center for Nano-Optoelectronics, School of Physics, Peking University, Beijing 100871, China*

Yulu Qin − *State Key Laboratory for Mesoscopic Physics, Collaborative Innovation Center of Quantum Matter, Frontiers Science Center for Nano-Optoelectronics, School of Physics, Peking University, Beijing 100871, China*

Guanyu Zhang − *State Key Laboratory for Mesoscopic Physics, Collaborative Innovation Center of Quantum Matter, Frontiers Science Center for Nano-Optoelectronics, School of Physics, Peking University, Beijing 100871, China*

Xiaoming Song − *State Key Laboratory of Precision Measurement Technology and Instruments, School of Precision Instruments and Optoelectronics Engineering, Tianjin University, Tianjin 300072, China*

Qihuang Gong − *State Key Laboratory for Mesoscopic Physics, Collaborative Innovation Center of Quantum Matter, Frontiers Science Center for Nano-Optoelectronics, School of Physics, Peking University, Beijing 100871, China; Collaborative Innovation Center of Extreme Optics, Shanxi University, Taiyuan, Shanxi 030006, China; Peking University Yangtze Delta Institute of Optoelectronics, Nantong, Jiangsu 226010, China*

Complete contact information is available at: https://pubs.acs.org/10.1021/acs.nanolett.2c03574

Author Contributions

#Z.X., Z.F., and X.L. contributed equally to this work. G.L. and D.S. conceived the idea and designed the experiments. Z.X. carried out FDTD simulations, performed FIB etching, analyzed the results, and wrote the manuscript. Z.F. and X.S. performed the SPCM measurements. X.L. and G.Z. fabricated the Cd_3As_2 photodetector. Z.X., Y.L., and Y.Q. performed the PEEM measurements. Z.L., D.S., G.L., and Q.G. discussed the results and promoted the manuscript presentation.

Notes

The authors declare no competing financial interest.

■ ACKNOWLEDGMENTS

This work was supported by the Guangdong Major Project of Basic and Applied Basic Research (Grant No. 2020B0301030009), the National Key Research and Development Program of China (Grant No. 2018YFB2200401, 2020YFA0308800, 2021YFA1400100), the National Natural Science Foundation of China (Grant Nos. 12034001, 91950111 and 11527901) and Beijing Natural Science Foundation (Grant Nos. JQ19001).

■ REFERENCES

(1) Liang, T.; Gibson, Q.; Ali, M. N.; Liu, M.; Cava, R. J.; Ong, N. P. Ultrahigh mobility and giant magnetoresistance in the Dirac semimetal Cd_3As_2. *Nat. Mater.* **2015**, *14* (3), 280−284.

(2) Neupane, M.; Xu, S.-Y.; Sankar, R.; Alidoust, N.; Bian, G.; Liu, C.; Belopolski, I.; Chang, T.-R.; Jeng, H.-T.; Lin, H.; Bansil, A.; Chou, F.; Hasan, M. Z. Observation of a three-dimensional topological Dirac semimetal phase in high-mobility Cd_3As_2. *Nat. Commun.* **2014**, *5* (1), 1−8.

(3) Liu, Z. K.; Jiang, J.; Zhou, B.; Wang, Z. J.; Zhang, Y.; Weng, H. M.; Prabhakaran, D.; Mo, S. K.; Peng, H.; Dudin, P.; Kim, T.; Hoesch, M.; Fang, Z.; Dai, X.; Shen, Z. X.; Feng, D. L.; Hussain, Z.; Chen, Y. L. A Stable three-dimensional topological Dirac semimetal Cd_3As_2. *Nat. Mater.* **2014**, *13* (7), 677−681.

(4) Yang, M.; Wang, J.; Han, J.; Ling, J.; Ji, C.; Kong, X.; Liu, X.; Huang, Z.; Gou, J.; Liu, Z.; Xiu, F.; Jiang, Y. Enhanced performance of wideband room temperature photodetector based on Cd_3As_2 thin film/pentacene heterojunction. *ACS Photonics* **2018**, *5* (8), 3438−3445.

(5) Huang, Z.; Jiang, Y.; Han, Q.; Yang, M.; Han, J.; Wang, F.; Luo, M.; Li, Q.; Zhu, H.; Liu, X.; Gou, J.; Wang, J. High responsivity and fast UV−vis−short-wavelength IR photodetector based on Cd_3As_2/MoS_2 heterojunction. *Nanotechnology* **2020**, *31* (6), 064001.

(6) Nair, R. R.; Blake, P.; Grigorenko, A. N.; Novoselov, K. S.; Booth, T. J.; Stauber, T.; Peres, N. M. R.; Geim, A. K. Fine structure constant defines visual transparency of graphene. *Science* **2008**, *320* (5881), 1308.

(7) Sun, D.; Aivazian, G.; Jones, A. M.; Ross, J. S.; Yao, W.; Cobden, D.; Xu, X. Ultrafast hot-carrier-dominated photocurrent in graphene. *Nat. Nanotechnol.* **2012**, *7* (2), 114−118.

(8) Sun, D.; Wu, Z.-K.; Divin, C.; Li, X.; Berger, C.; de Heer, W. A.; First, P. N.; Norris, T. B. Ultrafast relaxation of excited Dirac fermions

in epitaxial graphene using optical differential transmission spectroscopy. *Phys. Rev. Lett.* **2008**, *101* (15), 157402.
(9) Xue, Z.; Liao, X.; Li, Y.; Hu, A.; Chen, J.; Tang, J.; Yang, H.; Liao, Z.-M.; Lu, G.; Gong, Q. Photoexcited electron dynamics in Cd_3As_2 revealed by time- and energy-resolved photoemission electron microscopy. *J. Phys. Chem. C* **2022**, *126* (6), 3134−3139.
(10) Lu, W.; Ling, J.; Xiu, F.; Sun, D. Terahertz probe of photoexcited carrier dynamics in the Dirac semimetal Cd_3As_2. *Phys. Rev. B* **2018**, *98* (10), 104310.
(11) Lu, W.; Ge, S.; Liu, X.; Lu, H.; Li, C.; Lai, J.; Zhao, C.; Liao, Z.; Jia, S.; Sun, D. Ultrafast relaxation dynamics of photoexcited Dirac fermions in the three-dimensional Dirac semimetal Cd_3As_2. *Phys. Rev. B* **2017**, *95* (2), 024303.
(12) Wang, L.-X.; Li, C.-Z.; Yu, D.-P.; Liao, Z.-M. Aharonov−Bohm oscillations in Dirac semimetal Cd_3As_2 nanowires. *Nat. Commun.* **2016**, *7* (1), nl2c03574.
(13) Liu, J.; Xia, F.; Xiao, D.; García de Abajo, F. J.; Sun, D. Semimetals for high-performance photodetection. *Nat. Mater.* **2020**, *19* (8), 830−837.
(14) Lu, X.; Sun, L.; Jiang, P.; Bao, X. Progress of photodetectors based on the photothermoelectric effect. *Adv. Mater.* **2019**, *31* (50), 1902044.
(15) Li, G.; Zhang, H.; Li, Y.; Yin, S.; Kan, X.; Wei, W.; Du, H.; Ge, B.; An, C.; Tian, M.; Yan, F.; Yang, S.; Zhai, T.; Li, L. Ultrabroadband, fast, and polarization-sensitive photoresponse of low-symmetry 2D $NdSb_2$. *Nano Res.* **2022**, *15*, 5469−5475.
(16) Wang, Q.; Zheng, J.; He, Y.; Cao, J.; Liu, X.; Wang, M.; Ma, J.; Lai, J.; Lu, H.; Jia, S.; Yan, D.; Shi, Y.; Duan, J.; Han, J.; Xiao, W.; Chen, J.-H.; Sun, K.; Yao, Y.; Sun, D. Robust edge photocurrent response on layered type II Weyl semimetal WTe_2. *Nat. Commun.* **2019**, *10* (1), 1−7.
(17) Wang, Q.; Li, C.-Z.; Ge, S.; Li, J.-G.; Lu, W.; Lai, J.; Liu, X.; Ma, J.; Yu, D.-P.; Liao, Z.-M.; Sun, D. Ultrafast broadband photodetectors based on three-dimensional Dirac semimetal Cd_3As_2. *Nano Lett.* **2017**, *17* (2), 834−841.
(18) Liu, C.-H.; Chang, Y.-C.; Lee, S.; Zhang, Y.; Zhang, Y.; Norris, T. B.; Zhong, Z. Ultrafast lateral photo-Dember effect in graphene induced by nonequilibrium hot carrier dynamics. *Nano Lett.* **2015**, *15* (6), 4234−4239.
(19) Lu, W.; Fan, Z.; Yang, Y.; Ma, J.; Lai, J.; Song, X.; Zhuo, X.; Xu, Z.; Liu, J.; Hu, X.; Zhou, S.; Xiu, F.; Cheng, J.; Sun, D. Ultrafast photothermoelectric effect in Dirac semimetallic Cd_3As_2 revealed by terahertz emission. *Nat. Commun.* **2022**, *13* (1), 1623.
(20) Dai, W.; Liu, W.; Yang, J.; Xu, C.; Alabastri, A.; Liu, C.; Nordlander, P.; Guan, Z.; Xu, H. Giant photothermoelectric effect in silicon nanoribbon photodetectors. *Light Sci. Appl.* **2020**, *9* (1), 1−8.
(21) Buscema, M.; Barkelid, M.; Zwiller, V.; van der Zant, H. S. J.; Steele, G. A.; Castellanos-Gomez, A. Large and tunable photothermoelectric effect in single-layer MoS_2. *Nano Lett.* **2013**, *13* (2), 358−363.
(22) Ma, J.; Gu, Q.; Liu, Y.; Lai, J.; Yu, P.; Zhuo, X.; Liu, Z.; Chen, J.-H.; Feng, J.; Sun, D. Nonlinear photoresponse of type-II Weyl semimetals. *Nat. Mater.* **2019**, *18* (5), 476−481.
(23) Ali, M. N.; Gibson, Q.; Jeon, S.; Zhou, B. B.; Yazdani, A.; Cava, R. J. The crystal and electronic structures of Cd_3As_2, the three-dimensional electronic analogue of graphene. *Inorg. Chem.* **2014**, *53* (8), 4062−4067.
(24) Lai, J.; Liu, X.; Ma, J.; Wang, Q.; Zhang, K.; Ren, X.; Liu, Y.; Gu, Q.; Zhuo, X.; Lu, W.; Wu, Y.; Li, Y.; Feng, J.; Zhou, S.; Chen, J.-H.; Sun, D. Anisotropic broadband photoresponse of layered type-II Weyl semimetal $MoTe_2$. *Adv. Mater.* **2018**, *30* (22), 1707152.
(25) Lai, J.; Liu, Y.; Ma, J.; Zhuo, X.; Peng, Y.; Lu, W.; Liu, Z.; Chen, J.; Sun, D. Broadband anisotropic photoresponse of the 'hydrogen atom' version type-II Weyl semimetal candidate $TaIrTe_4$. *ACS Nano* **2018**, *12* (4), 4055−4061.
(26) Zhuo, X.; Lai, J.; Yu, P.; Yu, Z.; Ma, J.; Lu, W.; Liu, M.; Liu, Z.; Sun, D. Dynamical evolution of anisotropic response of type-II Weyl semimetal $TaIrTe_4$ under ultrafast photoexcitation. *Light Sci. Appl.* **2021**, *10* (1), 1−8.
(27) Xue, Z.; Zheng, W.; Li, Y.; Xue, M.; Hu, A.; Chen, J.; Jia, S.; Tang, J.; Chen, J.; Du, J.; Gao, P.; Ren, M.; Wang, S.; Liu, Y.; Yang, H.; Liao, Z.; Lu, G.; Gong, Q. Ultraviolet/visible quasicylindrical waves on semimetal Cd_3As_2 nanoplates. *Adv. Photonics Res.* **2022**, *3* (4), 2100354.
(28) Li, C.-Z.; Wang, L.-X.; Liu, H.; Wang, J.; Liao, Z.-M.; Yu, D.-P. Giant negative magnetoresistance induced by the chiral anomaly in individual Cd_3As_2 nanowires. *Nat. Commun.* **2015**, *6* (1), 1−7.
(29) Wang, J.; Qin, L.; Xu, W. Flexible and high precision thermal metasurface. *Commun. Mater.* **2021**, *2* (1), 1−10.
(30) Zhou, T.; Zhang, C.; Zhang, H.; Xiu, F.; Yang, Z. Enhanced thermoelectric properties of the Dirac semimetal Cd_3As_2. *Inorg. Chem. Front.* **2016**, *3* (12), 1637−1643.
(31) Obraztsov, P. A.; Lyashenko, D.; Chizhov, P. A.; Konishi, K.; Nemoto, N.; Kuwata-Gonokami, M.; Welch, E.; Obraztsov, A. N.; Zakhidov, A. Ultrafast zero-bias photocurrent and terahertz emission in hybrid perovskites. *Commun. Phys.* **2018**, *1* (1), 1−7.
(32) Wang, Z.; Weng, H.; Wu, Q.; Dai, X.; Fang, Z. Three-dimensional Dirac semimetal and quantum transport in Cd_3As_2. *Phys. Rev. B* **2013**, *88* (12), 125427.
(33) Li, C.; Wang, H.; Wang, F.; Li, T.; Xu, M.; Wang, H.; Wang, Z.; Zhan, X.; Hu, W.; Shen, L. Ultrafast and broadband photodetectors based on a perovskite/organic bulk heterojunction for large-dynamic-range imaging. *Light Sci. Appl.* **2020**, *9* (1), 1−8.
(34) Kovaleva, N.; Fekete, L.; Chvostova, D.; Muratov, A. Morphology and optical properties of thin Cd_3As_2 films of a Dirac semimetal compound. *Metals* **2020**, *10* (10), 1398.
(35) Bauer, E. A Brief History of PEEM. *J. Electron Spectrosc. Relat. Phenom.* **2012**, *185* (10), 314−322.
(36) Li, Y.; Liu, W.; Wang, Y.; Xue, Z.; Leng, Y.-C.; Hu, A.; Yang, H.; Tan, P.-H.; Liu, Y.; Misawa, H.; Sun, Q.; Gao, Y.; Hu, X.; Gong, Q. Ultrafast electron cooling and decay in monolayer WS_2 revealed by time- and energy-resolved photoemission electron microscopy. *Nano Lett.* **2020**, *20* (5), 3747−3753.
(37) Li, Y.; Sun, Q.; Zu, S.; Shi, X.; Liu, Y.; Hu, X.; Ueno, K.; Gong, Q.; Misawa, H. Correlation between near-field enhancement and dephasing time in plasmonic dimers. *Phys. Rev. Lett.* **2020**, *124* (16), 163901.
(38) Spektor, G.; Kilbane, D.; Mahro, A. K.; Frank, B.; Ristok, S.; Gal, L.; Kahl, P.; Podbiel, D.; Mathias, S.; Giessen, H.; Meyer zu Heringdorf, F.-J.; Orenstein, M.; Aeschlimann, M. Revealing the subfemtosecond dynamics of orbital angular momentum in nanoplasmonic vortices. *Science* **2017**, *355* (6330), 1187−1191.
(39) Liu, W.; Li, Y.; Yu, H.; Wang, J.; Hu, A.; Jia, S.; Li, X.; Yang, H.; Dai, L.; Lu, G.; Liu, Y.; Wang, S.; Gong, Q. Imaging and controlling photonic modes in perovskite microcavities. *Adv. Mater.* **2021**, *33* (25), 2100775.
(40) Fitzgerald, J. P. S.; Word, R. C.; Saliba, S. D.; Könenkamp, R. Photonic near-field imaging in multiphoton photoemission electron microscopy. *Phys. Rev. B* **2013**, *87* (20), 205419.
(41) Sharma, N.; Bar-David, J.; Mazurski, N.; Levy, U. Metasurfaces for enhancing light absorption in thermoelectric photodetectors. *ACS Photonics* **2020**, *7* (9), 2468−2473.
(42) Lu, H.; Guo, X.; Zhang, J.; Zhang, X.; Li, S.; Yang, C. Asymmetric metasurface structures for light absorption enhancement in thin film silicon solar cell. *J. Opt.* **2019**, *21* (4), 045901.
(43) Lu, R.; Ge, C.-W.; Zou, Y.-F.; Zheng, K.; Wang, D.-D.; Zhang, T.-F.; Luo, L.-B. A localized surface plasmon resonance and light confinement-enhanced near-infrared light photodetector. *Laser Photonics Rev.* **2016**, *10* (4), 595−602.
(44) van Beijnum, F.; Rétif, C.; Smiet, C. B.; Liu, H.; Lalanne, P.; van Exter, M. P. Quasi-cylindrical wave contribution in experiments on extraordinary optical transmission. *Nature* **2012**, *492* (7429), 411−414.

https://doi.org/10.1021/acs.nanolett.2c03574
Nano Lett. 2022, 22, 8728−8734